processes

MDPI

Article

Gas Prediction in Tight Sandstone Reservoirs Based on a Seismic Dispersion Attribute Derived from Frequency-Dependent AVO Inversion

Laidong Hu [1], Mingchun Chen [1,2,*] and Han Jin [3]

[1] Sinopec Geophysical Corporation, Beijing 100013, China
[2] College of Geophysics, Chengdu University of Technology, Chengdu 610059, China
[3] College of Geoexploration Science and Technology, Jilin University, Changchun 130026, China
* Correspondence: yn-chenmc.osgc@sinopec.com

Abstract

Accurate gas prediction is crucial for identifying gas-bearing zones in tight sandstone reservoirs. Traditional seismic techniques, primarily grounded in elastic theory, often overlook inelastic dispersion effects inherent to such formations. To overcome this limitation, we introduce a gas prediction approach utilizing a dispersion attribute derived from frequency-dependent inversion based on an AVO equation parameterized by a gas indicator and related properties. Rock physics modeling, based on multi-scale fracture theory, reveals the frequency-dependent gas indicator is highly responsive to variations in porosity and gas saturation. Seismic AVO simulations exhibit distinguishable signatures corresponding to these variations, supporting the potential to estimate reservoir properties from pre-stack seismic data. Synthetic data tests confirm that the values of the proposed dispersion attribute increase with increasing porosity and gas saturation. Additionally, the calculated dispersion attribute exhibits a strong positive correlation with gas content, validating its effectiveness for gas evaluation. Field application results further demonstrate that the proposed dispersion attribute shows prominent anomalies in sandstone reservoirs with high gas content. Compared to the conventional P-wave dispersion attribute, the proposed dispersion attribute exhibits superior reliability in detecting gas-rich zones. These results demonstrate the utility of the method in predicting gas-bearing regions in tight sandstone reservoirs.

Keywords: tight sandstones; gas prediction; rock physics; seismic dispersion attribute; AVO

check for updates

Academic Editor: Qingbang Meng

Received: 30 April 2025
Revised: 20 June 2025
Accepted: 7 July 2025
Published: 10 July 2025

Citation: Hu, L.; Chen, M.; Jin, H. Gas Prediction in Tight Sandstone Reservoirs Based on a Seismic Dispersion Attribute Derived from Frequency-Dependent AVO Inversion. *Processes* **2025**, *13*, 2210. https://doi.org/10.3390/pr13072210

Copyright: © 2025 by the authors. Licensee MDPI, Basel, Switzerland. This article is an open access article distributed under the terms and conditions of the Creative Commons Attribution (CC BY) license (https://creativecommons.org/licenses/by/4.0/).

1. Introduction

With the continuous rise in global energy demand, tight sandstone gas reservoirs have emerged as a vital unconventional hydrocarbon resource, offering substantial exploration potential and favorable development prospects. The basis for high-quality tight sandstone reservoirs is significant gas enrichment, as sufficient gas accumulation is essential to sustain productivity. However, tight sandstone reservoirs are often characterized by low porosity, low permeability, intricate pore structures, and strong heterogeneity. Such geological complexities pose significant challenges to the accurate identification of sweet spots [1,2].

At present, the integration of rock physics methodologies provides an effective framework for quantifying fluid-related variations in elastic and seismic responses. Rock physics templates (RPTs) have been extensively utilized for the identification of porosity and fluid [3–6]. Additionally, numerous fluid indicators, derived from various combinations

of elastic parameters, have demonstrated success in identifying reservoir fluids [7–11]. Concurrently, the direct estimation of reservoir properties from pre-stack seismic data has gained prominence due to its potential to minimize cumulative interpretation errors. As a result, AVO equations incorporating different fluid indicators have been developed to facilitate the direct inversion of reservoir parameters [12–17].

The aforementioned approaches primarily depend on elastic properties for fluid prediction. However, numerous studies have shown that gas saturation and porosity can induce observable seismic wave dispersion and attenuation. Laboratory experiments have validated the significant influence of fluids on P-wave velocity dispersion and attenuation behavior [18]. Concurrently, several theories have been proposed to describe frequency-dependent velocity variations resulting from fluid mobility within hydrocarbon-bearing formations [19–23]. Moreover, studies that integrate rock physics with seismic forward modeling have revealed that fluid-induced dispersion and attenuation exert notable effects on AVO responses [24,25]. These findings suggest that incorporating seismic wave dispersion into the development of seismic analysis methods offers a promising avenue for improving gas detection in tight sandstone reservoirs.

Contemporary seismic analysis techniques often utilize a frequency-dependent amplitude variation with offset (FD-AVO) methods to extract dispersion attributes from seismic data. The foundational FD-AVO framework was initially proposed by Wilson [26], and subsequent developments have introduced a range of dispersion attributes linked to P-wave reflection behavior [27–36] and fluid bulk modulus variations [37,38], primarily aimed at hydrocarbon detection. In recent years, machine learning methods have been incorporated into the framework of the FD-AVO inversion method [39,40]. Nonetheless, a key limitation of these existing approaches is their predominant focus on fluid effects while neglecting the influence of porosity in gas prediction. To achieve a more accurate evaluation of gas content, it is crucial to design dispersion attributes that account for the combined influence of fluid properties and porosity. The aforementioned approaches have been applied across different lithologies, including carbonates [3–5], sandstone [6,9–15,17,18,28–31,33,35,37–40], shale [27,34], and volcanic rocks [32,36]. Furthermore, seismic methods for fluid detection in various reservoirs have been thoroughly summarized and reviewed [41].

This study introduces a method for gas prediction in tight sandstone reservoirs using seismic dispersion attributes derived from a FD-AVO inversion method. Initially, an FD-AVO inversion framework is established by extending an AVO equation parameterized by a gas indicator and other elastic properties into the frequency domain to extract a dispersion attribute linked to gas content. The effectiveness of the proposed dispersion attribute for gas content identification is then assessed using synthetic seismic data. Subsequently, the method is applied to field data for gas prediction, with well log-derived gas content values serving to validate the reliability of the inversion results. Finally, a comparative analysis is conducted to demonstrate the advantages of the proposed dispersion attribute over conventional P-wave velocity dispersion.

2. Methods

2.1. FD-AVO Inversion of Dispersion Attribute D_F for Gas Prediction

Figure 1 illustrates the framework for extracting the dispersion attribute D_F using the FD-AVO inversion method. Based on the traditional P-wave reflection coefficient equation, a new AVO equation parameterized by indicators of gas content, porosity, and related elastic parameters has been proposed. Subsequently, the pre-stack seismic data are subjected to spectral decomposition. The resulting spectral components are used to compute the dispersion attribute D_F through the FD-AVO inversion method.

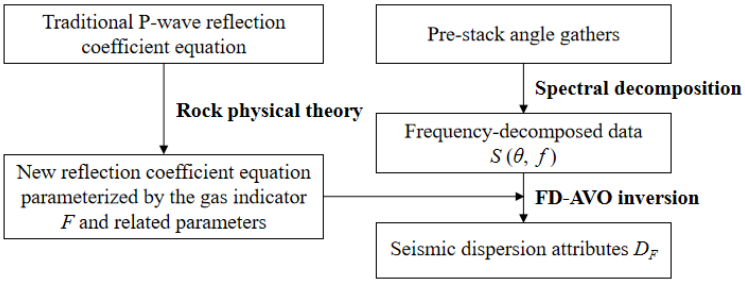

Figure 1. Framework for extracting the dispersion attribute D_{F} based on the FD-AVO inversion method.

Jin et al. [17] introduced a gas indicator F for the prediction of gas content in tight sandstones:

$$F = \frac{1}{K_{\mathrm{f}}\mu} \tag{1}$$

where K_{f} represents the fluid bulk modulus and μ denotes the shear modulus of the rock skeleton. Based on this, an AVO approximation was proposed to enable the direct inversion of the indicator F:

$$\begin{aligned} R_{\mathrm{PP}}(\theta) &= -\frac{\left(1+\tan^2\theta\right)\left(\gamma_{sat}^2-\gamma_{dry}^2\right)}{4\gamma_{sat}^2}\frac{\Delta F}{F} - \frac{\left(1+\tan^2\theta\right)\left(\gamma_{sat}^2-2\gamma_{dry}^2\right)+8\sin^2\theta}{2\gamma_{sat}^2}\frac{\Delta(\phi I_S)}{\phi I_S} \\ &+ \left[\frac{\left(1+\tan^2\theta\right)\left(\gamma_{sat}^2-\gamma_{dry}^2\right)+4\sin^2\theta}{2\gamma_{sat}^2} - \frac{\tan^2\theta}{2}\right]\frac{\Delta\rho}{\rho} \\ &+ \frac{\left(1+\tan^2\theta\right)\left(3\gamma_{sat}^2-5\gamma_{dry}^2\right)+16\sin^2\theta}{4\gamma_{sat}^2}\frac{\Delta\phi}{\phi} \end{aligned} \tag{2}$$

where I_{S} is the S-wave impedance, ρ represents density, ϕ is porosity, and θ denotes incidence angle; γ_{sat} and γ_{dry} are the P- and S-wave velocity ratio of saturated rock and dry frame, respectively.

Based on Equation (2), the frequency-dependent AVO equation can be expressed as follows:

$$R_{\mathrm{PP}}(\theta,\omega) \approx R_{\mathrm{PP}}(\theta,\omega_0) + A(\theta)(\omega-\omega_0)D_{\mathrm{F}} + B(\theta)(\omega-\omega_0)D_{\phi I_{\mathrm{S}}} \tag{3}$$

where

$$A(\theta) = -\frac{\left(1+\tan^2\theta\right)\left(\gamma_{\mathrm{sat}}^2-\gamma_{\mathrm{dry}}^2\right)}{4\gamma_{\mathrm{sat}}^2} \tag{4}$$

$$B(\theta) = -\frac{\left(1+\tan^2\theta\right)\left(\gamma_{\mathrm{sat}}^2-2\gamma_{\mathrm{dry}}^2\right)+8\sin^2\theta}{2\gamma_{\mathrm{sat}}^2} \tag{5}$$

$$D_{\mathrm{F}} = \frac{\partial}{\partial\omega}\left(\frac{\Delta F}{F}\right) \tag{6}$$

$$D_{\phi I_{\mathrm{S}}} = \frac{\partial}{\partial\omega}\left[\frac{\Delta(\phi I_{\mathrm{S}})}{\phi I_{\mathrm{S}}}\right] \tag{7}$$

Derivations from Equation (2) to (7) are provided in Appendix A.

2.2. Multi-Scale Fracture Theory

Within the multi-scale fracture theory proposed by Chapman [42,43], the effective stiffness matrix for an equivalent medium containing pores, microcracks, and fractures is expressed as follows:

$$C_{\mathrm{ijkl}} = C_{\mathrm{ijkl}}^0 - \phi_{\mathrm{p}}C_{\mathrm{ijkl}}^1 - \varepsilon_{\mathrm{c}}C_{i\mathrm{ijkl}}^2 - \varepsilon_{\mathrm{f}}C_{\mathrm{ijkl}}^3 \tag{8}$$

where $C^0{}_{ijkl}$ corresponds to the isotropic background stiffness coefficient; $C^1{}_{ijkl}$, $C^2{}_{ijkl}$, and $C^3{}_{ijkl}$ characterize the contributions of pore, microcrack, and fracture, respectively; ϕ_p represents porosity; ε_c quantifies microcrack density; and ε_f describes fracture density.

Scanning Electron Microscopy (SEM) analysis (Figure 2a) of the study area reveals a variety of pore types within the tight sandstones, including dissolution-enhanced intragranular pores, dissolved intergranular pores, and tectonic fractures. This pore system can be effectively modeled using a dual-porosity approach, where total porosity (ϕ) is partitioned into spherical pores (ϕ_p) and microcrack porosity (ϕ_c), as illustrated in Figure 2b. Accordingly, Equation (8) can be simplified by omitting the large-scale fracture parameter ε_f:

$$C_{ijkl} = C^0_{ijkl} - \phi_p C^1_{iijk} - \varepsilon_c C^2_{ijkl} \tag{9}$$

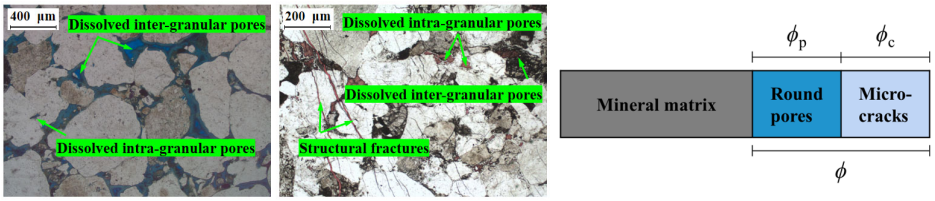

Figure 2. (**a**) SEM micrographs and (**b**) conceptual model of tight sandstones in the study area.

The frequency-dependent P-wave velocity $V_P(\omega)$ and S-wave velocity $V_S(\omega)$ are obtained from the stiffness components $C_{3333}(\omega)$ and $C_{4444}(\omega)$ in Equation (9):

$$V_P(\omega) = \sqrt{\frac{C_{3333}(\omega)}{\rho_s}} \tag{10}$$

$$V_S(\omega) = \sqrt{\frac{C_{2323}(\omega)}{\rho_s}} \tag{11}$$

where ρ_s denotes the density of the fluid-saturated tight sandstone.

3. Results

3.1. Synthetic Data Tests

Based on the multi-scale fracture theory outlined in Section 2.2, we quantitatively analyze the frequency-dependent characteristics of the elastic wave velocity and the indicator F in tight sandstone reservoirs. Figure 3a shows the computed V_P dispersion curves at three different porosity (ϕ) values while maintaining a constant gas saturation (S_g). The corresponding frequency-dependent variations in the indicator F are presented in Figure 3b. The analysis reveals that the dispersion characteristics gradually intensify as porosity increases.

Figure 4 further explores the frequency-dependent V_P and F characteristics under varying S_g conditions, with a constant ϕ. Both V_P and F exhibit notable frequency-dependent variations as S_g increases. The observed frequency-dependent behaviors of V_P and F under different gas saturations and porosities provide valuable insights for gas prediction using seismic dispersion attributes.

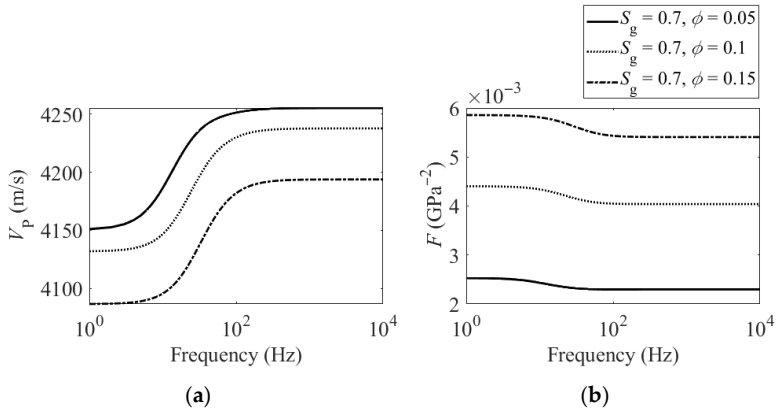

Figure 3. Frequency-dependent (**a**) V_P and (**b**) F in tight sandstones under different ϕ conditions with a fixed S_g = 0.7.

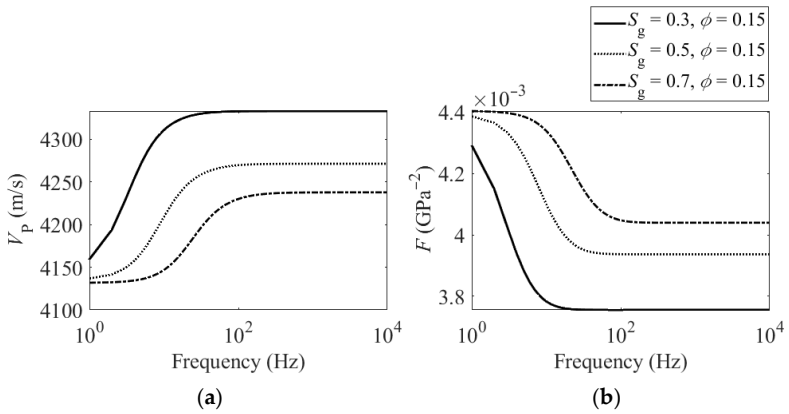

Figure 4. Frequency-dependent (**a**) V_P and (**b**) F in tight sandstones under different S_g conditions with a fixed ϕ = 0.15.

Moreover, the efficacy of the proposed dispersion attributes derived from FD-AVO inversion is validated through synthetic data tests. A layered model of a tight sandstone layer encased in mudstone is depicted in Figure 5. The P-wave velocity, S-wave velocity, and density of the mudstone are 4200 m/s, 2000 m/s, and 2600 kg/m^3, respectively. In contrast, the P-wave velocity, S-wave velocity, and density of the tight sandstone are 4500 m/s, 2200 m/s, and 2460 kg/m^3. Synthetic seismic data are generated by integrating the propagator matrix method with rock physics modeling [44,45]. The tight sandstone reservoir is modeled with a thickness of 10 m. For seismic simulation, a Ricker wavelet with a central frequency of 40 Hz is employed, and the incidence angles range up to 30°.

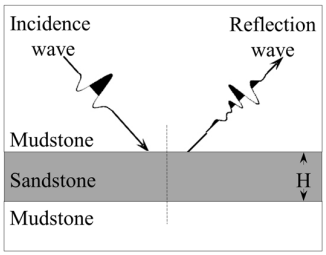

Figure 5. Theoretical model for synthetic data tests. H represents the thickness of the tight sandstone reservoir.

Figure 6a–c show the simulated AVO responses for three reservoir models with different porosities (ϕ = 0.05, 0.1, and 0.15) at a fixed gas saturation (S_g = 0.7). The tight

sandstone reflection signatures exhibit clear angle-dependent amplitude variations. Analysis reveals that reflection amplitudes attenuate with an increasing incidence angle across all porosity conditions. Additionally, models with higher porosity show enhanced amplitude attenuation at higher angles, indicating porosity-dependent AVO response characteristics. Figure 6d presents the variations in the dispersion attribute D_F for the three models with different porosities. The inversion process was carried out using the method outlined in Section 2.1, with a frequency bandwidth of 5–100 Hz. Quantitative analysis shows more pronounced D_F responses in models with higher porosity in the tight sandstone.

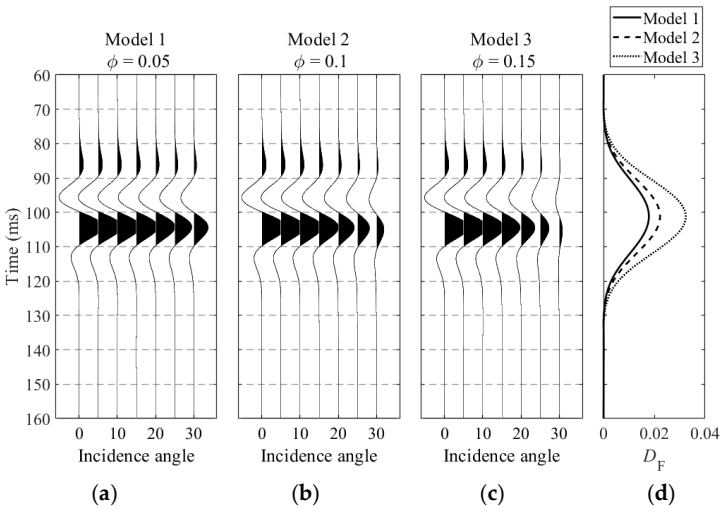

Figure 6. Synthetic AVO data at different ϕ conditions with fixed S_g = 0.7: (**a**) ϕ = 0.05, (**b**) ϕ = 0.1, and (**c**) ϕ = 0.15; (**d**) D_F values computed from the synthetic data in (**a**–**c**).

Figure 7a–c present the modeled AVO responses for distinct gas saturation values (S_g = 0.3, 0.5, and 0.7) at a fixed porosity (ϕ = 0.15). The analysis reveals that waveform polarity reversals occur at high incidence angles for the low gas saturation model (S_g = 0.3). Additionally, reflection amplitudes increase at higher angles for models with higher S_g values. Figure 7d shows the calculated D_F values, which progressively increase with higher S_g conditions.

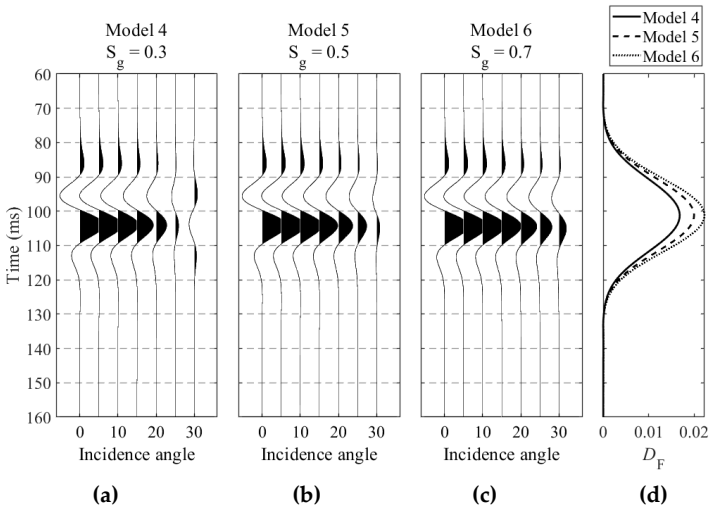

Figure 7. Synthetic AVO data at different S_g conditions with fixed ϕ = 0.15: (**a**) S_g = 0.3, (**b**) S_g = 0.5, and (**c**) S_g = 0.7; (**d**) D_F values computed from the synthetic data in (**a**–**c**).

Figure 8 further illustrates the root-mean-square (RMS) magnitudes of the dispersion attribute D_F under conditions of varying ϕ and S_g. The D_F response shows a clear en-

hancement with increasing values of both ϕ and S_g, indicating its dependence on these parameters. This behavior supports the conclusion that D_F serves as an effective indicator for estimating gas content ($S_g \times \phi$).

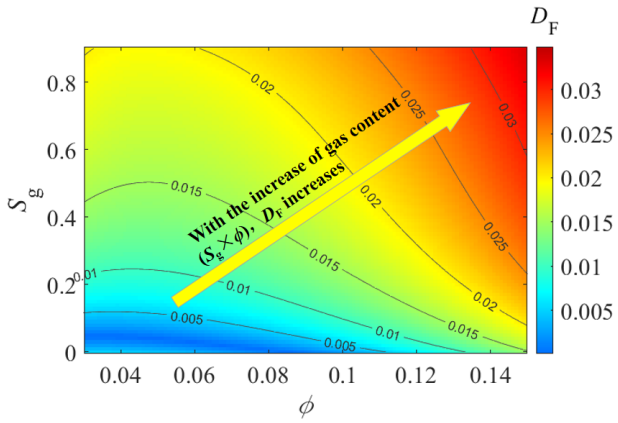

Figure 8. Computed D_F for varying S_g and ϕ.

Furthermore, the dispersion attribute D_F, computed for varying S_g and ϕ conditions in Figure 8, is transformed into a cross-plot of D_F versus $S_g \times \phi$, as shown in Figure 9. The relationship demonstrates a nonlinear growth pattern, characterized by an initial steep increase followed by a more gradual rise. The red trendline represents the central tendency, and these results confirm a distinct positive correlation between D_F and $S_g \times \phi$.

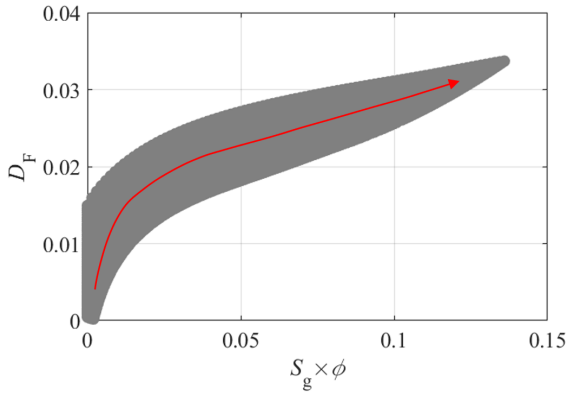

Figure 9. Cross-plot between D_F and $S_g \times \phi$, derived from the conversion of the result in Figure 7. The red arrow indicates the trend of D_F varying with $S_g \times \phi$.

3.2. Real Data Applications

The methodology developed in this study is applied to field data from a tight sandstone gas reservoir. Figure 10 shows the two-way travel time (TWT) contours of the target reservoir horizon. The TWT distribution reveals a relatively smooth structural relief across the study area, with three gas-producing wells (B, C, and D) and two no gas-producing wells (A and E) indicated.

Figures 11–13 present comparative analyses of logging data, cross-well pre-stack seismic traces, predicted dispersion attribute D_F, D_{Vp} results, and the volumetric fraction of minerals for the three wells. The elastic properties of clay and quartz are shown in Table 1 [46]. The seismic inversion process utilizes a frequency bandwidth of 5–100 Hz. The frequency range used is optimized empirically, according to the bandwidth and characteristics of real seismic data. Notably, compared to D_{Vp}, the seismically derived D_F shows a strong agreement with logging data for gas content ($S_g \times \phi$). The intuitive comparison results confirm the superiority of D_F over D_{Vp}. The target intervals with high $S_g \times \phi$

values can be consistently identified by high-value D_F anomalies. In comparison, Figure 14 presents a cross-plot of $S_g \times \phi$ versus V_P/V_S and $S_g \times \phi$ versus $\lambda\rho$, demonstrating that the conventional elastic parameters V_P/V_S and $\lambda\rho$ show less sensitivity in effectively indicating gas content. These results emphasize the potential of D_F as a more effective indicator for identifying gas-bearing zones than both D_{Vp} and traditional elastic parameters.

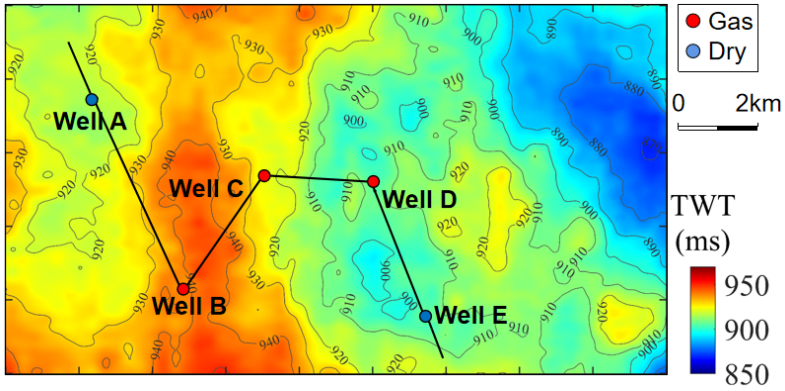

Figure 10. Two-way travel time (TWT) map for the target tight sandstone gas reservoir.

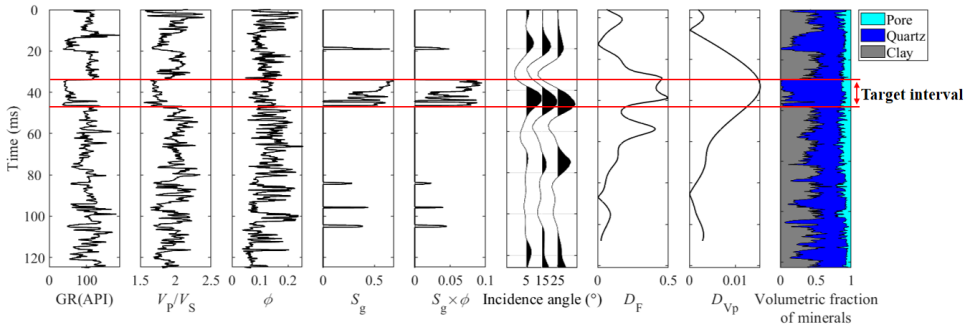

Figure 11. Curves of gamma ray (GR), V_P/V_S, ϕ, S_g, $S_g \times \phi$, cross-well pre-stack seismic traces, D_F, D_{Vp}, and volumetric fraction of minerals for well B.

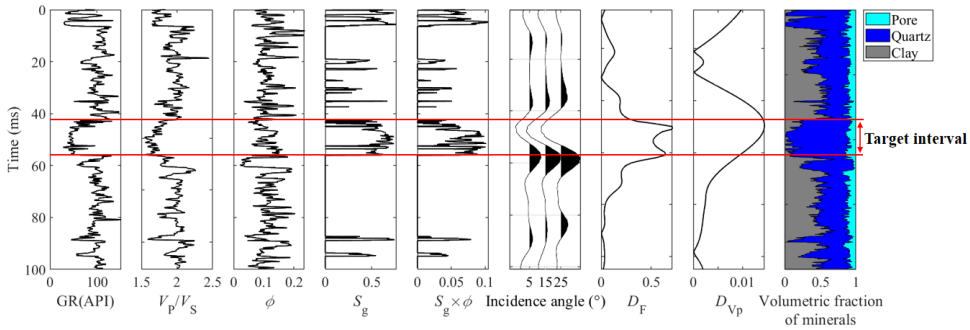

Figure 12. Curves of gamma ray (GR), V_P/V_S, ϕ, S_g, $S_g \times \phi$, cross-well pre-stack seismic traces, D_F, D_{Vp}, and volumetric fraction of minerals for well C.

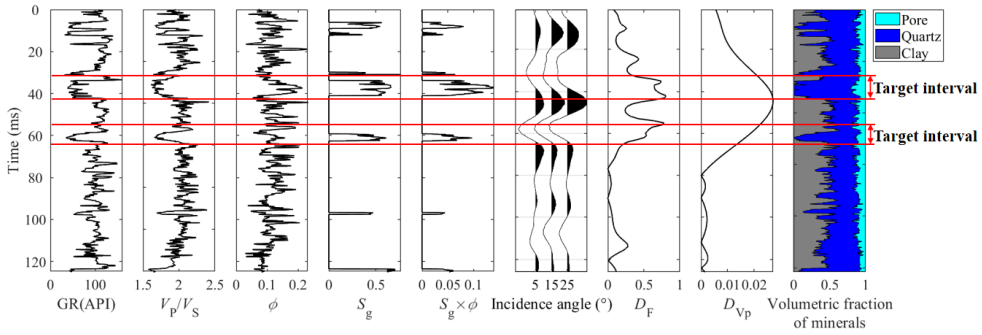

Figure 13. Curves of gamma ray (GR), V_P/V_S, ϕ, S_g, $S_g \times \phi$, cross-well pre-stack seismic traces, D_F, D_{Vp}, and volumetric fraction of minerals for well D.

Table 1. The properties of clay and quartz.

	Clay	Quartz
V_P (km/s)	3.90	6.05
V_S (km/s)	1.50	3.90
ρ (g/cm^3)	2.58	2.65

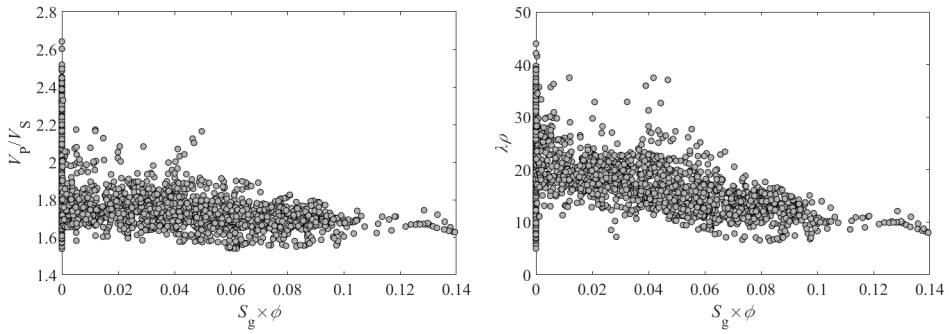

Figure 14. Cross-plot of (**a**) $S_g \times \phi$ and V_P/V_S, and (**b**) $S_g \times \phi$ and $\lambda\rho$.

Figure 15 presents the seismic profile across wells A, B, and C, with the bounding surfaces of the target reservoir delineated by two black horizons. Additionally, Figure 16 shows the corresponding time–frequency analysis results obtained through continuous wavelet transform (CWT), displaying spectral decompositions at six discrete frequencies: 10, 20, 30, 40, 50, and 60 Hz. These spectrally decomposed seismic attributes serve as the foundational data for FD-AVO inversion.

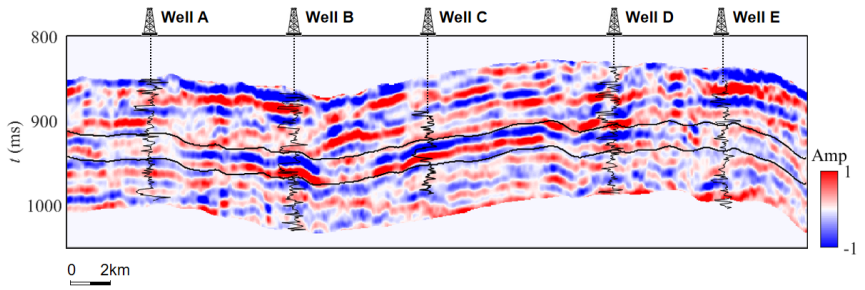

Figure 15. Seismic profile across Wells A, B, C, D, and E with superimposed GR logging curves.

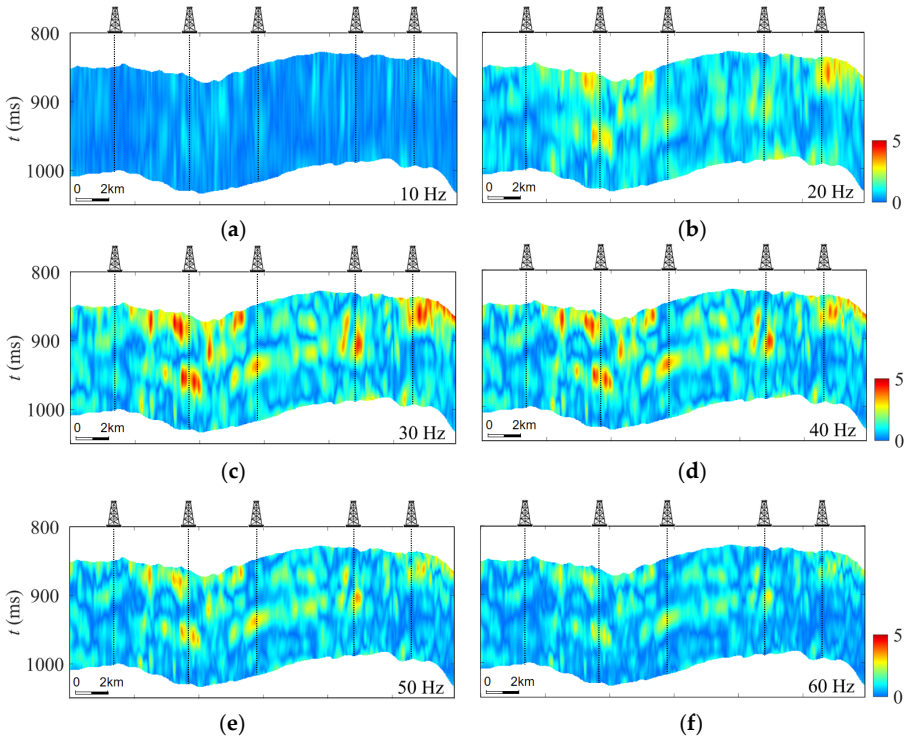

Figure 16. Spectral decomposition results of the seismic profile in Figure 15 at the following frequencies: (**a**) 10 Hz, (**b**) 20 Hz, (**c**) 30 Hz, (**d**) 40 Hz, (**e**) 50 Hz, and (**f**) 60 Hz.

For comparison, Figures 17 and 18 show the dispersion attributes D_{F} calculated using the method presented in this study and D_{Vp} derived from the conventional framework [34]. Figures 19 and 20 display the $V_{\mathrm{P}}/V_{\mathrm{S}}$ and $\lambda\rho$, both computed from the elastic inversion results. The results are superimposed with $S_{\mathrm{g}} \times \phi$ logging data. It is observed that gas-bearing tight sandstone formations within the target zones exhibit high D_{F} and D_{Vp} and low $V_{\mathrm{P}}/V_{\mathrm{S}}$ and $\lambda\rho$ responses. In comparison, D_{F} anomalies demonstrate an improved sensitivity to the zones with high gas content than D_{Vp}, $V_{\mathrm{P}}/V_{\mathrm{S}}$, and $\lambda\rho$, as evidenced by the close alignment between elevated D_{F} values and productive intervals with high $S_{\mathrm{g}} \times \phi$ in Wells B, C, and D. Meanwhile, the tight formations in dry wells A and E with very low $S_{\mathrm{g}} \times \phi$ show no D_{F} anomalies in the target interval.

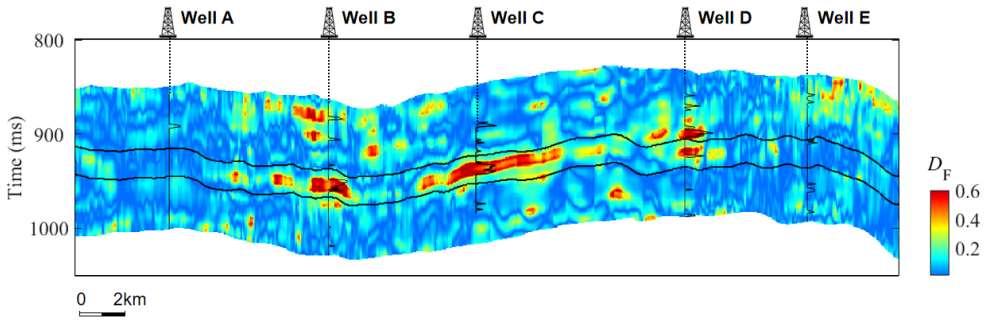

Figure 17. Profile of D_{F} across Wells A, B, C, D, and E with superimposed $S_{\mathrm{g}} \times \phi$ logging data.

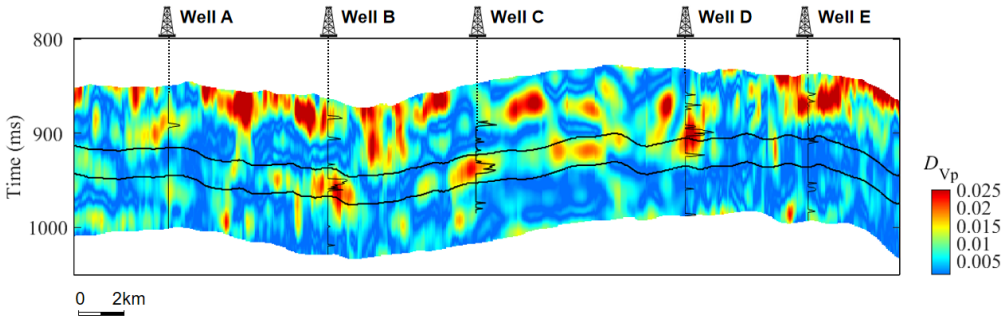

Figure 18. Profile of D_{Vp} across Wells A, B, C, D, and E with superimposed $S_g \times \phi$ logging data.

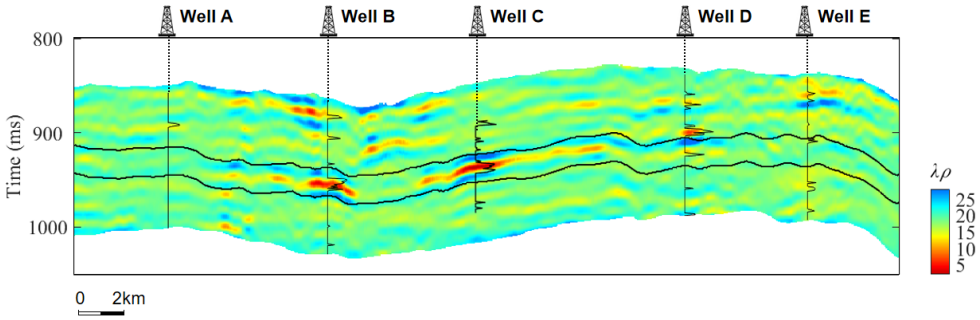

Figure 19. Profile of V_P/V_S across Wells A, B, C, D, and E with superimposed $S_g \times \phi$ logging data.

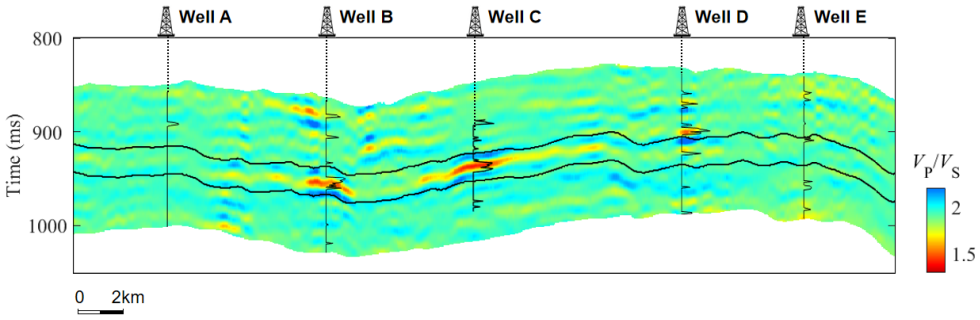

Figure 20. Profile of $\lambda\rho$ across Wells A, B, C, D, and E with superimposed $S_g \times \phi$ logging data.

4. Discussion

Accurate gas prediction is crucial for delineating gas-bearing zones in tight sandstone reservoirs. This study proposes a gas prediction methodology utilizing a dispersion attribute derived from frequency-dependent inversion. To verify the effectiveness of the proposed method with the theoretical test, this study adopts the multi-scale fracture theory [42,43] to calculate the frequency-dependent P-wave and S-wave velocities, which are then used to generate synthetic data. The multi-scale fracture theory primarily focuses on the dispersion mechanism caused by fluid squirt flow within complex pore structures. In future research, additional rock physics models can be incorporated to investigate other dispersion mechanisms. Using multi-scale fracture theory, we conducted rock physics modeling to analyze the frequency-dependent characteristics of indicator F under different porosity and gas saturation conditions [Figure 3b]. The modeling results reveal the significant sensitivity of indicator F to variations in both ϕ and S_g. However, conventional seismic inversion and interpretation methods have typically relied on elastic theories for fluid identification, overlooking inelastic dispersion effects in tight sandstone reservoirs. To address these challenges, this paper presented a frequency-dependent pre-stack inversion method to extract seismic dispersion attributes, enhancing gas prediction by utilizing

the inelastic properties of tight sandstones. This method is based on an AVO equation specifically parameterized by the gas indicator F and associated properties.

As demonstrated in Figures 6a–c and 7a–c, we simulated and analyzed the seismic AVO responses of tight sandstone reservoirs with varying ϕ and S_g configurations by integrating rock physics modeling with the propagator matrix method. In these simulations, the tight sandstone exhibits inelastic properties due to fluid flow within multi-scale fracture systems. The results revealed distinct AVO signatures associated with variations in ϕ and S_g, indicating the feasibility of identifying porosity and fluid using pre-stack seismic data. Furthermore, based on the method outlined in Section 2.1, we computed the seismic dispersion attribute D_F for gas content ($S_g \times \phi$) assessment in tight sandstones. Synthetic data tests validated the capability of the proposed D_F for reliably estimating variations in ϕ and S_g [Figures 6d and 7d]. Quantitative analysis systematically demonstrated a significant increase in D_F values with higher ϕ and S_g values (Figure 8), confirming the sensitivity of D_F to both parameters. Notably, D_F exhibited a clear positive correlation with the product $S_g \times \phi$, as shown in Figure 9, further supporting its reliability for gas content assessment.

Finally, the proposed method and dispersion attribute D_F were applied to field data for gas prediction in the study area, as shown in Figure 10. As illustrated in Figures 11–13, the results indicate that the seismically derived D_F demonstrates a strong correlation with the well log-derived $S_g \times \phi$. Target sandstones with high $S_g \times \phi$ values were identified by high-value D_F anomalies in all three wells. These findings support the feasibility of using D_F as a reliable indicator for predicting gas-bearing tight sandstones in the investigated region. Comparative analysis further revealed that D_F anomalies (Figure 17) exhibit a significantly stronger correlation with gas-enriched intervals than the conventional P-wave dispersion attribute D_{Vp} (Figure 18), confirming the superior reliability of D_F for gas content prediction in tight sandstones.

Seismic elastic inversion and quantitative seismic interpretation methods have been employed to estimate porosity and gas saturation [4,6,17]. Different from the aforementioned conventional elastic inversion approaches, this study proposes a dispersion attribute obtained from frequency-dependent inversion. A key advantage of this method lies in its utilization of inelastic properties derived from seismic frequency information, offering a method for characterizing gas content ($S_g \times \phi$). However, the presented dispersion attribute provides a qualitative evaluation of gas content. Future research could focus on developing quantitative indicators to achieve a more accurate characterization of reservoir properties by using formal uncertainty quantification methods such as the Bayesian inversion or Monte Carlo simulations.

Meanwhile, rock physics modeling approaches that account for various factors such as mineralogical heterogeneity and elastic–inelastic coupling effects may be incorporated, offering deeper insights into the seismic dispersion characteristics associated with porosity and fluid. In addition, further research will explore the simultaneous inversion for multiple reservoir parameters (such as porosity, gas saturation, and fluid type) and combine seismic dispersion attributes with other seismic indicators to enhance predictive reliability and compensate the limitations of single-attribute approaches. Finally, the proposed method can be further applied to diverse geological settings, reservoir types, and well data in further study.

5. Conclusions

This study presents a gas prediction methodology based on a dispersion attribute derived from frequency-dependent inversion, utilizing an AVO equation specifically parameterized by the gas indicator F and associated properties. Rock physics modeling, grounded in multi-scale fracture theory, demonstrated the significant sensitivity of the

frequency-dependent indicator F to variations in both porosity (ϕ) and gas saturation (S_g). Seismic AVO modeling results revealed distinct signatures linked to variations in ϕ and S_g, suggesting the feasibility of predicting porosity and fluid using pre-stack seismic data. Synthetic data tests confirmed the ability of the proposed seismic dispersion attribute D_F to reliably estimate variations in ϕ and S_g. Moreover, D_F showed a clear positive correlation with the product of $S_g \times \phi$, underscoring its effectiveness in gas content evaluation. Field data applications indicated that target sandstones with high well log-derived $S_g \times \phi$ values were identified by elevated D_F anomalies. Comparative analysis further demonstrated that D_F anomalies exhibited a significantly stronger correlation with gas-enriched intervals than the conventional P-wave dispersion attribute D_{Vp}, validating the superior reliability of D_F for gas content prediction in tight sandstones. These findings suggest that the proposed seismic dispersion attribute provides an effective indicator for identifying gas-bearing areas in tight sandstones.

Author Contributions: Conceptualization, L.H., M.C. and H.J.; methodology, H.J.; software, H.J.; validation, M.C. and H.J.; formal analysis, L.H., M.C. and H.J.; investigation, L.H., M.C. and H.J.; resources, L.H. and M.C.; data curation, H.J.; writing—original draft preparation, L.H., M.C. and H.J.; writing—review and editing, L.H., M.C. and H.J.; visualization, H.J.; supervision, L.H. and M.C.; project administration, L.H. and M.C. All authors have read and agreed to the published version of the manuscript.

Funding: This research was funded by the National Natural Science Foundation of China, grant numbers 42274160 and 42074153.

Data Availability Statement: The datasets presented in this article are not readily available because they are not permitted to be shared.

Conflicts of Interest: Authors Laidong Hu and Mingchun Chen were employed by the company Sinopec Geophysical Corporation. The remaining authors declare that the research was conducted in the absence of any commercial or financial relationships that could be construed as a potential conflict of interest.

Nomenclature

AVO	Amplitude variation with offset
FD-AVO	Frequency-dependent amplitude variation with offset
K_f	Fluid bulk modulus
μ	Shear modulus of rock skeleton
F	Gas indicator
I_S	S-wave impedance
ρ	Density
ϕ	Porosity
θ	Incidence angle
γ_{sat}	P- and S-wave velocity ratio of saturated rock
γ_{dry}	P- and S-wave velocity ratio of dry frame
ω_0	Reference frequency
D_F	Dispersion attribute related to gas content
$D_{\phi IS}$	Dispersion attribute related to porosity and S-wave impedance
ΔS	Decomposed spectral components
ΔR	Reflection coefficient difference term
W	Wavelet spectrum
$C^0{}_{ijkl}$	Isotropic background stiffness coefficients
$C^1{}_{ijkl}$	The contributions of pore to stiffness coefficients
$C^2{}_{ijkl}$	The contributions of microcrack to stiffness coefficients
$C^3{}_{ijkl}$	The contributions of fracture to stiffness coefficients

ϕ_P	Porosity
ε_c	Microcrack density
ε_f	Fracture density
$V_P(\omega)$	Frequency-dependent P-wave velocity
$V_S(\omega)$	Frequency-dependent S-wave velocity
ρ_s	Density of the fluid-saturated tight sandstone

Appendix A

Jin et al. [17] introduced a gas indicator F for the prediction of gas content in tight sandstones:

$$F = \frac{1}{K_f \mu} \tag{A1}$$

where K_f represents the fluid bulk modulus and μ denotes the shear modulus of the rock skeleton. Based on this, a new AVO approximation was proposed to enable the direct inversion of the indicator F:

$$\begin{aligned} R_{PP}(\theta) &= -\frac{\left(1+\tan^2\theta\right)\left(\gamma_{sat}^2-\gamma_{dry}^2\right)}{4\gamma_{sat}^2}\frac{\Delta F}{F} - \frac{\left(1+\tan^2\theta\right)\left(\gamma_{sat}^2-2\gamma_{dry}^2\right)+8\sin^2\theta}{2\gamma_{sat}^2}\frac{\Delta(\phi I_S)}{\phi I_S} \\ &+ \left[\frac{\left(1+\tan^2\theta\right)\left(\gamma_{sat}^2-\gamma_{dry}^2\right)+4\sin^2\theta}{2\gamma_{sat}^2} - \frac{\tan^2\theta}{2}\right]\frac{\Delta\rho}{\rho} \\ &+ \frac{\left(1+\tan^2\theta\right)\left(3\gamma_{sat}^2-5\gamma_{dry}^2\right)+16\sin^2\theta}{4\gamma_{sat}^2}\frac{\Delta\phi}{\phi} \end{aligned} \tag{A2}$$

where I_S is the S-wave impedance, ρ represents density, ϕ is porosity, and θ denotes incidence angle; γ_{sat} and γ_{dry} are the P- and S-wave velocity ratio of saturated rock and dry frame, respectively.

Additionally, the frequency-dependent behavior of the indicators F and I_S is incorporated, while density ρ and ϕ are reasonably assumed to remain constant across different frequencies ω [38]. This assumption facilitates the derivation of the FD-AVO equation, expressed as follows:

$$R_{PP}(\theta,\omega) = A(\theta)\frac{\Delta F}{F}(\omega) + B(\theta)\frac{\Delta(\phi I_S)}{\phi I_S}(\omega) + C(\theta)\frac{\Delta\rho}{\rho} + D(\theta)\frac{\Delta\phi}{\phi} \tag{A3}$$

where

$$A(\theta) = -\frac{\left(1+\tan^2\theta\right)\left(\gamma_{sat}^2-\gamma_{dry}^2\right)}{4\gamma_{sat}^2} \tag{A4}$$

$$B(\theta) = -\frac{\left(1+\tan^2\theta\right)\left(\gamma_{sat}^2-2\gamma_{dry}^2\right)+8\sin^2\theta}{2\gamma_{sat}^2} \tag{A5}$$

$$C(\theta) = -\frac{\left(1+\tan^2\theta\right)\left(\gamma_{sat}^2-\gamma_{dry}^2\right)+4\sin^2\theta}{2\gamma_{sat}^2} - \frac{\tan^2\theta}{2} \tag{A6}$$

$$D(\theta) = -\frac{\left(1+\tan^2\theta\right)\left(3\gamma_{sat}^2-5\gamma_{dry}^2\right)+16\sin^2\theta}{4\gamma_{sat}^2} \tag{A7}$$

By applying a first-order Taylor series expansion to Equation (A3) around a reference frequency ω_0, the following expression is obtained:

$$R_{PP}(\theta,\omega) \approx R_{PP}(\theta,\omega_0) + (\omega-\omega_0)A(\theta)\frac{\partial}{\partial\omega}\left(\frac{\Delta F}{F}\right) + (\omega-\omega_0)B(\theta)\frac{\partial}{\partial\omega}\left[\frac{\Delta(\phi I_S)}{\phi I_S}\right] \tag{A8}$$

where

$$R_{\mathrm{PP}}(\theta,\omega_0) = A(\theta)\frac{\Delta F}{F}(\omega_0) + B(\theta)\frac{\Delta(\phi I_{\mathrm{S}})}{\phi I_{\mathrm{S}}}(\omega_0) + C(\theta)\frac{\Delta\rho}{\rho} + D(\theta)\frac{\Delta\phi}{\phi} \tag{A9}$$

The dispersion attributes corresponding to F and ϕI_{S} are defined as follows:

$$D_{\mathrm{F}} = \frac{\partial}{\partial\omega}\left(\frac{\Delta F}{F}\right) \tag{A10}$$

$$D_{\phi\mathrm{I_S}} = \frac{\partial}{\partial\omega}\left[\frac{\Delta(\phi I_{\mathrm{S}})}{\phi I_{\mathrm{S}}}\right] \tag{A11}$$

Meanwhile, by defining

$$\Delta R_{\mathrm{PP}}(\theta,\omega) = R_{\mathrm{PP}}(\theta,\omega) - R_{\mathrm{PP}}(\theta,\omega_0) \tag{A12}$$

Equation (A8) can be reformulated as follows:

$$\Delta R_{\mathrm{PP}}(\theta,\omega) = (\omega-\omega_0)\left[A(\theta)D_{\mathrm{F}} + B(\theta)D_{\phi\mathrm{Is}}\right] \tag{A13}$$

Building upon Equation (A13), the inversion framework for dispersion attributes D_{F} and $D_{\phi\mathrm{Is}}$ can be expressed in matrix form to facilitate the application to real seismic data:

$$d = G\begin{bmatrix} D_{\mathrm{F}} \\ D_{\phi\mathrm{Is}} \end{bmatrix} \tag{A14}$$

where

$$d = \begin{bmatrix} \Delta S(\theta_1,\omega_1) \\ \vdots \\ \Delta S(\theta_1,\omega_{\mathrm{m}}) \\ \vdots \\ \vdots \\ \Delta S(\theta_{\mathrm{n}},\omega_1) \\ \vdots \\ \Delta S(\theta_{\mathrm{n}},\omega_{\mathrm{m}}) \end{bmatrix} \tag{A15}$$

$$G = \begin{bmatrix} W(\omega_1)(\omega_1-\omega_0)A(\theta_1) & W(\omega_1)(\omega_1-\omega_0)B(\theta_1) \\ \vdots & \vdots \\ W(\omega_{\mathrm{m}})(\omega_{\mathrm{m}}-\omega_0)A(\theta_1) & W(\omega_{\mathrm{m}})(\omega_{\mathrm{m}}-\omega_0)B(\theta_1) \\ \vdots & \vdots \\ \vdots & \vdots \\ W(\omega_1)(\omega_1-\omega_0)A(\theta_{\mathrm{n}}) & W(\omega_1)(\omega_1-\omega_0)B(\theta_{\mathrm{n}}) \\ \vdots & \vdots \\ W(\omega_{\mathrm{m}})(\omega_{\mathrm{m}}-\omega_0)A(\theta_{\mathrm{n}}) & W(\omega_{\mathrm{m}})(\omega_{\mathrm{m}}-\omega_0)B(\theta_{\mathrm{n}}) \end{bmatrix} \tag{A16}$$

The decomposed spectral components ΔS in Equation (A15) are related to the reflection coefficient difference term ΔR in Equation (A13) through incorporating the wavelet spectral matrix [$W(\omega_1)$, $W(\omega_2)$, . . ., and $W(\omega_{\mathrm{m}})$] shown in Equation (A16).

References

1. Liu, L.; Tang, D.Z.; Wo, Y.J.; Liu, L.H.; Sun, W.; Lu, H.M.; Yekikang, M.Q. Favorable area prediction of tight sandstone: A case study of the He8 formation in the Kangning area, Eastern Ordos Basin, China. *J. Pet. Sci. Eng.* **2019**, *175*, 430–443.
2. Shu, Y.; Sang, S.X.; Lin, Y.X.; Zhou, X.Z.; Wang, H.; Wang, Z.L. The influence of magmatic-hydrothermal activities on porosity and permeability of sandstone reservoirs in the Linxing area, Ordos Basin, Northern China. *J. Asian Earth Sci.* **2021**, *213*, 104741. [CrossRef]
3. Ba, J.; Cao, H.; Carcione, J.M.; Tang, G.; Yan, X.F.; Sun, W.T.; Nie, J.X. Multiscale rock-physics templates for gas detection in carbonate reservoirs. *J. Appl. Geophys.* **2013**, *93*, 77–82. [CrossRef]
4. Pang, M.Q.; Ba, J.; Carcione, J.M.; Picotti, S.; Zhou, J.; Jiang, R. Estimation of porosity and fluid saturation in carbonates from rock-physics templates based on seismic Q. *Geophysics* **2019**, *84*, M25–M36. [CrossRef]
5. Pang, M.Q.; Ba, J.; Fu, L.Y.; Carcione, J.M.; Markus, U.I.; Zhang, L. Estimation of microfracture porosity in deep carbonate reservoirs based on 3D rock-physics templates. *Int. J. Subsurf. Charact.* **2021**, *8*, SP43–SP52. [CrossRef]
6. Guo, Z.Q.; Qin, X.Y.; Liu, C. Quantitative characterization of tight gas sandstone reservoirs using seismic data via an integrated rock-physics-based framework. *Pet. Sci.* **2023**, *20*, 3428–3440. [CrossRef]
7. Goodway, W.N.; Chen, T.; Downton, J. Improved AVO fluid detection and lithology discrimination using Lamé petrophysical parameters; "λρ", μρ, λ/μ Fluid Stack," from P and S inversions. In Proceedings of the 67th SEG Annual Meeting, Dallas, TX, USA, 2–7 November 1997; pp. 183–186.
8. Quakenbush, M.; Shang, B.; Tuttle, C. Poisson impedance. *Lead. Edge* **2006**, *25*, 128–138. [CrossRef]
9. Xu, C.X.; Ma, P.S.; Lai, L.B.; Sun, Y.H.; Li, Z.C. Sensitivity parameters of tight sand gas: A case study of Lower Cretaceous Yingcheng Formation of Yingtai gas field in Songliao Basin, NE China. *Pet. Explor. Dev.* **2014**, *41*, 712–716. [CrossRef]
10. Huang, X.R.; Huang, J.P.; Li, Z.C. High-Sensitivity Fluid Identification Factor in Anisotropic Tight-Oil Sandstone Reservoirs. In *SEG Annual Meeting*; SEG: Houston, TX, USA, 2015; pp. 2688–2692.
11. Wang, P.; Chen, X.H.; Li, X.Y.; Cui, Y.A.; Li, J.Y.; Wang, B.F. Analysis and Estimation of an Inclusion-Based Effective Fluid Modulus for Tight Gas-Bearing Sandstone Reservoirs. *IEEE. Trans. Geosci. Remote Sens.* **2022**, *60*, 4502710. [CrossRef]
12. Yin, X.Y.; Zhang, S.X.; Zhang, F. Two-term elastic impedance inversion and Russell fluid factor direct estimation method for deep reservoir fluid identification. *Chin. J. Geophys.* **2013**, *7*, 2378–2390.
13. Zong, Z.Y.; Yin, X.Y. Direct inversion of Young's and Poisson impedances for fluid discrimination. *Geofluids* **2017**, *16*, 1006–1016. [CrossRef]
14. Jia, L.Y.; Li, L.; Wang, Q.Y.; Ma, J.F.; Wang, H.F.; Wang, D.X. Fluid identification factor inversion based on generalized elastic impedance. *Geophys. Prospect. Pet.* **2018**, *57*, 302–311.
15. Gao, G.; Yang, Y.H.; Zhao, B.; Duan, H.L.; Wang, X.Y.; Wei, Y.Z. A method for establishing and directly extracting sensitive identification factors of unconsolidated sandstones. *Oil Geophys. Prospect.* **2019**, *54*, 1329–1338.
16. Ma, Z.Q.; Yin, X.Y.; Zong, Z.Y.; Tan, Y.Y.; Ji, L.X.; Yang, Z.F.; Yan, X.F. Sequential Bayesian seismic inversion for fracture parameters and fluid indicator in tilted transversely isotropic media. *Geophysics* **2023**, *88*, R355–R371. [CrossRef]
17. Jin, H.; Liu, C.; Guo, Z.Q. Gas prediction in tight sandstones based on the rock-physics-derived seismic amplitude variation versus offset method. *Pet. Sci.* **2024**, *21*, 3951–3964. [CrossRef]
18. Yin, H.j.; Zhao, J.G.; Tang, G.Y.; Zhao, L.M.; Ma, X.Y.; Wang, S.X. Pressure and fluid effect on frequency-dependent elastic moduli in fully saturated tight sandstone. *J. Geophys. Res. Solid Earth* **2017**, *122*, 8925–8942. [CrossRef]
19. Chapman, M.; Liu, E.; Li, X. The influence of fluid-sensitive dispersion and attenuation on AVO analysis. *Geophys. J. Int.* **2006**, *167*, 89–105. [CrossRef]
20. Chapman, M. Modeling the effect of multiple sets of mesoscale fractures in porous rock on frequency-dependent anisotropy. *Geophysics* **2009**, *74*, D97–D103. [CrossRef]
21. Ba, J.; Carcione, J.M.; Cao, H.; Du, Q.Z.; Yuan, Z.Y.; Lu, M.H. Velocity dispersion and attenuation of P waves in partially-saturated rocks: Wave propagation equations in double-porosity medium. *Chin. J. Geophys.* **2012**, *55*, 219–231.
22. Ba, J.; Xu, W.H.; Fu, L.Y.; Carcione, J.M.; Zhang, L. Rock anelasticity due to patchy saturation and fabric heterogeneity: A double double-porosity model of wave propagation. *J. Geophys. Res. Solid Earth* **2017**, *122*, 1949–1976. [CrossRef]
23. Sun, W.T.; Ba, J.; Carcione, J.M. Theory of wave propagation in partially saturated double-porosity rocks: A triple-layer patchy model. *Geophys. J. Int.* **2016**, *205*, 22–37. [CrossRef]
24. He, Y.X.; Wu, X.Y.; Fu, K.; Zhou, D.; Wang, S.X. Modeling the Effect of Microscopic and Mesoscopic Heterogeneities on Frequency-Dependent Attenuation and Seismic Signatures. *IEEE. Trans. Geosci. Remote Sens. Lett.* **2018**, *15*, 1174–1178. [CrossRef]
25. He, Y.X.; Li, X.L.; Tang, G.Y.; Dong, C.H.; Chen, M.; Wang, S.X. Modeling the effects of fracture infill on frequency-dependent anisotropy and AVO response of a fractured porous layer. *Pet. Sci.* **2021**, *18*, 758–772. [CrossRef]
26. Wilson, A.; Chapman, M.; Li, X.Y. Frequency-dependent AVO inversion. In Proceedings of the 79th Annual International Meeting, SEG, Expanded Abstracts, Houston, TX, USA, 25–30 October 2009; pp. 341–345.

27. Pang, S.; Liu, C.; Guo, Z.Q.; Liu, X.W.; Liu, Y.W. Gas identification of shale reservoirs based on frequency-dependent AVO inversion of seismic data. *Chin. J. Geophys.* **2018**, *61*, 4613–4624.
28. Liu, W.; Cao, S.Y.; Jin, Z.Y.; Wang, Z.M.; Chen, Y.K. A novel hydrocarbon detection approach via high-resolution frequency-dependent AVO inversion based on variational mode decomposition. *IEEE. Trans. Geosci. Remote Sens.* **2018**, *56*, 2007–2024. [CrossRef]
29. Luo, C.; Li, X.Y.; Huang, G.T. Hydrocarbon identification by application of improved sparse constrained inverse spectral decomposition to frequency-dependent AVO inversion. *J. Geophys. Eng.* **2018**, *15*, 1446–1459. [CrossRef]
30. Huang, G.T.; Chen, X.H.; Luo, C.; Chen, Y.K. Mesoscopic Wave-Induced Fluid Flow Effect Extraction by Using Frequency-Dependent Prestack Waveform Inversion. *IEEE. Trans. Geosci. Remote Sens.* **2021**, *59*, 6510–6524. [CrossRef]
31. Jin, H.; Liu, C.; Guo, Z.Q.; Zhang, Y.M.; Niu, C.; Wang, D.; Ling, Y. Rock physical modeling and seismic dispersion attribute inversion for the characterization of a tight gas sandstone reservoir. *Front. Earth Sci.* **2021**, *9*, 641651. [CrossRef]
32. Guo, Z.Q.; Li, Y.D.; Liu, C.; Zhang, D.; Li, A.B. Characterization of a Volcanic Gas Reservoir Using Seismic Dispersion and Fluid Mobility Attributes. *Lithosphere* **2021**, *3*, 9520064. [CrossRef]
33. Guo, Z.Q.; Zhao, D.Y.; Liu, C. Gas prediction using an improved seismic dispersion attribute inversion for tight sandstone gas reservoirs in the Ordos Basin, China. *J. Nat. Gas. Sci. Eng.* **2022**, *101*, 104499. [CrossRef]
34. Guo, Z.Q.; Zhang, X.D.; Liu, C.; Liu, X.W.; Liu, Y.W. Hydrocarbon Identification and Bedding Fracture Detection in Shale Gas Reservoirs Based on a Novel Seismic Dispersion Attribute Inversion Method. *Surv. Geophys.* **2022**, *43*, 1793–1816. [CrossRef]
35. Luo, X.; Chen, X.H.; Lv, B.N.; Liu, J.J.; Wu, H.J.; Wang, P. Frequency-Dependent AVO Inversion Using a Modified Window-Parameter-Optimized S-Transform for High Gas-Saturation Reservoir Delineation. *IEEE. Trans. Geosci. Remote Sens. Lett.* **2023**, *20*, 3000805. [CrossRef]
36. Li, Y.D.; Guo, Z.Q.; Liu, C. Characterization of Fluid-Saturated Fractures Based on Seismic Azimuthal Anisotropy Dispersion Inversion Method. *IEEE. Trans. Geosci. Remote Sens.* **2024**, *62*, 1–17. [CrossRef]
37. Wang, P.; Li, J.; Chen, X.H.; Wang, K.D.; Wang, B.F. Fluid Discrimination Based on Frequency-Dependent AVO Inversion with the Elastic Parameter Sensitivity Analysis. *Feofluis* **2019**, *2019*, 1–14. [CrossRef]
38. Guo, Z.Q.; Zhao, D.Y.; Liu, C. A New Seismic Inversion Scheme Using Fluid Dispersion Attribute for Direct Gas Identification in Tight Sandstone Reservoirs. *Remote Sens.* **2022**, *14*, 5326. [CrossRef]
39. Tian, Y.; Gao, J.; Stovas, A.; Meng, C. Frequency-dependent AVO inversion via deep neural network and application on tight reservoir parameters prediction. In Proceedings of the 84th EAGE Annual Conference and Exhibition, Vienna, AT, USA, 5–8 June 2023.
40. Tian, Y.J.; Stovas, A.; Gao, J.H.; Meng, C.J.; Yang, C. Frequency-Dependent AVO Inversion and Application on Tight Sandstone Gas Reservoir Prediction Using Deep Neural Network. *IEEE. Trans. Geosci. Remote Sens.* **2023**, *61*, 1–13. [CrossRef]
41. Fawad, M.; Hansen, J.A.; Mondol, N.H. Seismic-fluid detection-a review. *Earth Sci. Rev.* **2020**, *210*, 103347. [CrossRef]
42. Chapman, M.; Zatsepin, S.v.; Crampin, S. Derivation of a microstructural poroelastic model. *Geophys. J. Int.* **2002**, *151*, 427–451. [CrossRef]
43. Chapman, M. Frequency-dependent anisotropy due to meso-scale fractures in the presence of equant porosity. *Geophys. Prospect.* **2003**, *51*, 369–379. [CrossRef]
44. Guo, Z.Q.; Liu, C.; Li, X.Y.; Lan, H.T. An Improved Method for the Modeling of Frequency-Dependent Amplitude-Versus-Offset Variations. *IEEE. Geosci. Remote Sens. Lett.* **2015**, *12*, 63–67.
45. Guo, Z.Q.; Liu, X.W. Seismic rock physics characterization of anisotropic shale-a Longmaxi Shale case study. *J. Geophys. Eng.* **2018**, *15*, 512–526. [CrossRef]
46. Mavko, G.; Mukerji, T.; Dvorkin, J. *The Rock Physics Handbook: Tools for Seismic Analysis in Porous Media*; Cambridge University Press: Cambridge, UK, 2009.

Disclaimer/Publisher's Note: The statements, opinions and data contained in all publications are solely those of the individual author(s) and contributor(s) and not of MDPI and/or the editor(s). MDPI and/or the editor(s) disclaim responsibility for any injury to people or property resulting from any ideas, methods, instructions or products referred to in the content.